



Nanoscale

**Facilitated Transport Membrane with Functionalized Ionic
Liquid Carriers for CO₂/N₂, CO₂/O₂, and CO₂/Air
Separations**

Journal:	<i>Nanoscale</i>
Manuscript ID	NR-ART-06-2022-003214.R1
Article Type:	Paper
Date Submitted by the Author:	11-Aug-2022
Complete List of Authors:	Lee, Yun-Yang; Case Western Reserve University, Chemical and Biomolecular Engineering Wickramasinghe, Nalinda; Case Western Reserve University, Department of Chemistry Dikki, Ruth; Case Western Reserve University Jan, Darrell; National Aeronautics and Space Administration, Ames Research Center Gurkan, Burcu; Case Western Reserve University, Chemical and Biomolecular Engineering

SCHOLARONE™
Manuscripts

1 **Facilitated Transport Membrane with Functionalized Ionic Liquid Carriers for CO₂/N₂, CO₂/O₂,**
2 **and CO₂/Air Separations**

3

4 Yun-Yang Lee¹, Nalinda P. Wickramasinghe², Ruth Dikki¹, Darrell L. Jan³, Burcu Gurkan^{1,*}

5

6 1. Department of Chemical and Biomolecular Engineering, Case Western Reserve University,
7 Cleveland, OH

8 2. Northeast Ohio High Field NMR Facility, Case Western Reserve University, Cleveland, OH

9 3. Ames Research Center, National Aeronautics and Space Administration, Moffett Field, CA

10

11

12 **Keywords**

13 Direct air capture; carbon capture; gas separation; CO₂ selectivity; poly(ionic liquid); graphene
14 oxide; composite membranes

15

16 **Abstract**

17 CO₂ separations from cabin air and the atmospheric air are challenged by the very low partial
18 pressures of CO₂. In this study, a facilitated transport membrane (FTM) is developed to separate
19 CO₂ from air using functionalized ionic liquid (IL) and poly(ionic liquid) (PIL) carriers. A highly
20 permeable bicontinuous structured poly(ethersulfone)/poly(ethylene terephthalate) (*bPES/PET*)
21 substrate is used to support the PIL-IL impregnated graphene oxide thin film. The CO₂ separation
22 performance was tested under a mixture feed of CO₂/N₂/O₂/H₂O. Under 410 ppm of CO₂ at 1
23 atm, CO₂ permeance of 3923 GPU, and CO₂/N₂ and CO₂/O₂ selectivities of 1200 and 300,
24 respectively, are measured with helium sweeping on the permeate side. For increased
25 transmembrane pressure (> 0 atm), a thicker PIL-IL/GO layer was needed to provide mechanical
26 strength and prevent leaching of the mobile carrier. CO₂ binding to the carriers, ion diffusivities,
27 and the glass transition temperature of the PIL-IL gels were examined to determine the
28 membrane composition and explain the separation performance. This report represents the first
29 FTM study with PIL-IL carriers for CO₂ separation from air.

1 INTRODUCTION

2 Removal of metabolically generated carbon dioxide (CO₂) from cabin air in spacecrafts (2500 ppm
3 CO₂)¹ is accomplished by sorbents like zeolites^{1,2} which have high CO₂ capacities. However,
4 zeolites, similar to most common metal organic frameworks³, are not selective to CO₂ especially
5 in the presence of moisture and their generation requires significant thermal energy.
6 Furthermore, the temperature swing between room temperature and 300-350 °C creates cracks
7 in the zeolite pellets and dusting.⁴ The dusting is problematic because it can migrate to small
8 passages, where it can lodge and causes clogging. This is of particular concern in spacecraft since
9 the dust migration in microgravity will be different from what can be observed in ground tests.
10 Therefore, it is desired to develop new sorbents and less energy demanding separation
11 technologies. Similarly, CO₂ capture from the atmospheric air, referred as the direct air capture
12 (DAC), relies on the selective capture of CO₂ from a very dilute concentration (410 ppm CO₂) and
13 sequestration of the captured CO₂ in order to achieve negative emissions. While carbon capture
14 and sequestration is more efficient to implement at point sources of CO₂ emissions, such as
15 power plants, petroleum refinery, and chemical plants where CO₂ concentration is higher; there
16 is still considerable amount of CO₂ being emitted from discrete sources that are difficult to
17 decarbonize such as transportation (29 %), commercial and residential buildings (13%), and
18 agricultural activities (10 %) that total up to 52% of the overall CO₂ emissions.⁵ Therefore, carbon
19 negative technologies such as DAC is essential to stay below the projected 1.5 °C temperature
20 rise globally.⁶

21
22 Simple thermodynamical calculations (see SI) suggest that the theoretical minimum work for DAC,
23 where CO₂ is 410-420 ppm, is almost four times greater than that from post-combustion CO₂
24 capture (PCCC) where the CO₂ is about 20%. Accounting for the fluid transportation, compression,
25 heating, and thermal exchange, the overall energy demand for CO₂ separation from dilute stream
26 (e.g., 410 - 2500 ppm) is much greater than the theoretical work. The estimated energy
27 requirement for DAC (410 ppm) and space cabin air (2500 ppm) is in the range of 200 to 400 kJ
28 per mol CO₂⁷⁻¹⁰, whereas the energy for PCCC is roughly half of that¹⁰. The state-of-the-art DAC
29 technologies, with a few demonstrations in pilot scale¹¹, rely on either the solid adsorption or
30 liquid absorption of CO₂. Liquid systems pass air through solutions like aqueous amines¹² or alkali

1 metal hydroxides^{13,14} Solid systems utilize supported amine sorbents^{15–17} and humidity-swing
2 quaternary ammonium based anion-exchange resins^{18,19}. However, these sorption techniques
3 are energy-intensive processes, since the strong binding of amine and CO₂ (C-N bond, about -80
4 kJ/mol)²⁰ requires a temperature of around 120 °C to cleave off CO₂ for sorbent regeneration.
5 Similarly, the calcination temperature of above 700 °C for alkali/alkaline earth carbonates²¹
6 results in a high energy demand.

7
8 In contrast to absorption and adsorption technologies, membrane separation is a non-
9 equilibrium process that operates by mass control²² and under isothermal conditions with
10 typically higher energy efficiency. It is also a promising technology for its high modularity, process
11 simplicity, and lower operational cost.²³ Conventional solution-diffusion (S-D) gas separation
12 membranes rely on the difference in solubility and diffusivity of the target gas over other gas
13 components for separation.²⁴ Recent progresses on the S-D membranes focused on increasing
14 **(1)** the solubility selectivity toward CO₂ over other gases by the incorporation of highly polar or
15 ionic components^{25–29}; and **(2)** the diffusivity selectivity for CO₂ sieving by rigid polymeric
16 backbones with high free volume.^{30–34} There is usually a tradeoff between gas permeance and
17 selectivity of a membrane, as described by the Robeson upper-bound.^{35–37} The S-D type
18 membranes are often implemented as multi-stage membrane systems to achieve the desired
19 separation, which inevitably drives up the energy consumption. Facilitated transport membranes
20 (FTMs) utilize CO₂-philic carriers such as amines that chemically bind with CO₂, thus enabling CO₂
21 transport by both **(1)** vehicular motions (CO₂ transport in the form of CO₂-carrier complexes) and
22 **(2)** hopping motions (CO₂ transport via hopping along a number of CO₂-philic sites) of the carriers,
23 along with **(3)** CO₂ diffusion, following the direction of transmembrane CO₂ gradient.³⁸ Therefore,
24 the CO₂ permeation is significantly improved even under reduced CO₂ partial pressures while
25 maintaining a high selectivity.³⁹ Therefore, FTMs perform above the Robeson upper-bound.
26 Amine functionalized polymers are the most common FTMs that are referred as having fixed site
27 carriers. FTMs that incorporate amine-based salts and ionic liquids (ILs) as mobile carriers^{40–47} are
28 shown to further enhance CO₂ transport.⁴⁸

29

1 While FTMs have been studied for CO₂ separation from post-combustion flue gas, there are only
2 a few reports that we are aware of discussing their utility relevant for DAC and for CO₂ removal
3 from cabin air.^{49–51} Under DAC and cabin air conditions, there is very small driving force for CO₂
4 transport owing to low concentration, temperature, and humidity; hence, it is extremely
5 challenging to concentrate the CO₂ on the effluent side. There has been two reports assessing
6 membrane-based DAC processes by simulations based on **(1)** a hypothetical non-FTM⁵² with
7 ultra-high permeance (40,000 GPU) and low CO₂/N₂ selectivity (70); and **(2)** a hypothetical FTM⁵³
8 with high permeance (2500 GPU) and high CO₂/N₂ selectivity (680). In 2022, Sandru et al.
9 fabricated a three-layered composite membrane with an ultrathin surface-grown amine-rich top
10 layer (10 nm) and a thin mid-layer of highly permeable amorphous polytetrafluoroethylene, PTFE,
11 (1 μm) coated over a porous membrane support as the bottom layer (50 μm).⁵⁴ The fabricated
12 membrane achieved a CO₂ permeability of 1000 Barrer (equivalent to 50,000 GPU; calculated
13 based on the reported overall membrane thickness of 50 μm) and a CO₂/N₂ selectivity greater
14 than 1000, with a CO₂/N₂ feed (10/90 v/v; RH = 100 %) at 25 °C. The authors observed no diffusion
15 limitations, unlike the previously reported thicker polyallylamine FTM (1 μm in thickness; 300
16 GPU and selectivity of 23)⁵⁵. While this membrane was not tested under conditions relevant to
17 DAC or cabin air, it demonstrates the importance of a thin selective layer and a highly permeable
18 substrate to overcome the selectivity-permeability trade-off.

19
20 Lee and Gurkan reported a poly(ionic liquid) - ionic liquid / graphene oxide (PIL-IL/GO) composite
21 membrane in 2021 as the first representative FTM specifically designed for CO₂/N₂ separation
22 relevant to DAC and CO₂ removal from cabin air.⁵⁶ The PIL-IL carriers were nanoconfined within
23 the GO nano framework (GONF) resulting in a 900 nm-thick CO₂ selective layer on an
24 ultrafiltration (UF) membrane substrate. The choice of the mobile carrier, 1-methyl-3-
25 ethylimidazolium 2-cyanopyrrolide, [EMIM][2-CNpyr], enabled the reactivity-mobility balance of
26 CO₂ by synergizing the IL's high affinity to CO₂ and low viscosity (in comparisons to other reactive
27 ILs). A high CO₂ permeance of 3090 GPU coupled with a high CO₂/N₂ selectivity of 1180 was
28 demonstrated by the PIL-IL/GO FTM under 410 ppm CO₂ feed at 25 °C and 40% RH. This
29 performance is superior to other known polyvinylamine and PIL ionomer based FTMs under

1 similar conditions.^{40,47} Here, we extend this work and report a thin PIL-IL/GO selective layer on a
2 *b*PES/PET substrate with well-interconnected pores as highly permeable FTM that demonstrates
3 high performance of CO₂ separation from CO₂/N₂/O₂/H₂O mixture at extremely low CO₂ partial
4 pressures. The impacts of oxygen and water on CO₂ capacity and the diffusivity of the carrier
5 were examined by ¹³C-NMR and ¹H-DOSY NMR. The specific interactions between the GONF and
6 the PIL-IL gel was characterized by HSBC NMR and FTIR. This study reports on the CO₂/O₂
7 selectivity and tunability of the CO₂/(N₂+O₂) separation ratio and the mechanical strength against
8 a transmembrane pressure for PIL-IL/GO type FTMs through the PIL-IL composition and GONF
9 layer thickness.

1 EXPERIMENTAL SECTION

2 Materials

3 The IL precursor, 1-ethyl-3-methylimidazolium iodide ([EMIM][I], >98%) was purchased from TCI
4 America. The ACS grade reagent methanol, isopropanol, and acetone were purchased from Alfa
5 Aesar via Thermo Scientific. Anion precursor pyrrole-2-carbonitrile (99%) and Amberlite® IRN-78
6 anion exchange resin (AER) in [OH⁻] form were purchased from Thermo Scientific. The poly(ionic
7 liquid (PIL) precursor, poly(diallyldimethylammonium chloride) (P[DADMA][Cl], M_w 400-500 kDa,
8 ~20 wt.% aqueous solution) and paramagnetic compound chromium acetylacetonate (Cr(ACAC)₃,
9 97%) were purchased from Millipore-Sigma. The AER was washed with methanol for at least
10 three times and vacuum dried at room temperature before use. Solid P[DADMA][Cl] was acquired
11 by directly pulling vacuum on the aqueous solution at 40 °C for three days and 80 °C for a day.
12 The deuterated solvent DMSO-d₆ (25 ml, 99.8%) was purchased from Thermo Scientific. The NMR
13 tubes (5 mm OD; 7" L; wall thickness: 0.38 mm) with coded closed caps were purchased from
14 Bruker. The NMR coaxial tube set (inner cell: NE-5-CIC; outer cell: NE-UPE-7) were purchased
15 from New Era Enterprises, Inc.

16
17 The ultrafiltration (UF) substrate membrane (LY; nominal cutoff of 100kD) with
18 poly(ethersulfone) (PES) skin layer and poly(ethylene terephthalate) (PET) nonwoven substrate
19 was purchased from Synder Filtration. The *b*PES/PET was prepared following the procedure as
20 described by Pang et al.⁵⁷. Briefly, the highly gas permeable substrates with bicontinuous
21 structured skin layer (with pore size of 30-40 nm) were fabricated by water-vapor induced phase
22 separation, followed with water immersion. This highly permeable membrane is abbreviated as
23 *b*PES/PET to make a distinction from the commercial UF substrate. Single-layer graphene oxide
24 (GO) dispersion (5 mg/ml) was purchased from ACS Material (synthesized by modified Hummer's
25 method and have an average width and thickness of 0.3 μm and 0.8 nm, respectively).

26
27 Tank gases of nitrogen (N₂; Ultra High Purity (UHP)), argon (Ar; UHP), helium (He; UHP), carbon
28 dioxide (CO₂; bone dry), hydrogen (H₂; UHP), and synthetic air (synthetic blend of N₂ (80%) and
29 O₂ (20%), with less than 1 ppm of CO₂) were purchased from Airgas.

1

2 **Methods**3 **Synthesis of [EMIM][2-CNpyr] (IL) and P[DADMA][2-CNpyr] (PIL)**

4 The synthesis of IL and PIL started with the anion exchange step of the precursor materials of
5 [EMIM][I] (10 g in 100 ml methanol) and P[DADMA][Cl] (10 g in 100 ml methanol), respectively,
6 into OH⁻ intermediates. The use of AER to precursor was monitored to be around 5 mg AER per
7 mmole precursor. The residual halide content in the intermediate solution was tested by 0.1 N
8 silver nitrate (AgNO₃) solution and confirmed to be low (< 1000 ppm) from the lack of visual white
9 precipitates of silver halides. The halide contents were further determined to be lower than 0.25
10 % (detection limit) by combustion ion chromatography. The intermediate solutions of IL and PIL
11 in [OH]⁻ form were separately mixed with the anion precursor pyrrole 2-carbonitrile (with cation
12 to anion precursor molar ratio of 1:1.02 mol) for acid-base neutralization reaction to complete
13 overnight. The excess solvent was removed from the resulting solutions by rotary evaporation at
14 60 °C. Samples were then vacuum dried at 80 °C for overnight to remove residual water. The
15 molecular structure of the synthesized PIL and IL were characterized and confirmed by ¹H-NMR
16 and heteronuclear single quantum coherence (HSQC), heteronuclear multiple bond correlation
17 (HMBC) on a Bruker 500 MHz (**Figure S2** and **S2**).

18

19 **Fabrication of PIL-IL/GO Composite Membrane**

20 Both UF and *b*PES/PET membrane substrates were rinsed with methanol/DI water (1:1 v/v) for
21 at least three time to remove residual salt crystals from the substrate. This step is important as
22 these contaminants can change the surface charge of GO flakes in the suspension in the next
23 step, causing coagulation and failure of the GONF layer deposition. The membranes were dried
24 in vacuum at 40 °C overnight prior to use. The GO in water dispersion (0.2 mg/ml and 2 mg /ml)
25 were prepared by diluting the purchased GO solution (5 mg/ml) with DI water and sonication.
26 The GONF layer was deposited over the substrates by vacuum filtering the GO suspension on top
27 of the membrane substrate (with level accuracy checked) for roughly 5-10 min. To ensure even
28 coverage and a final GONFL layer with homogenous thickness, the leveling of the membrane was
29 confirmed to be perfectly horizontal. The deposited GONF layer was then impregnated by the

1 PIL-IL gel by drop casting. The PIL-IL casting solution was prepared by mixing 0.2 mg/ml of PIL and
2 20 mg/ml of IL in methanol. The fabricated PIL-IL/GO on *b*PES/PET membranes were allowed to
3 dry under ambient air and were kept under vacuum at ambient temperature before use.

4

5 **Materials Characterization**

6 The Fourier-Transformed Infrared (FTIR) spectra of the IL, PIL, and membranes were taken on
7 Nicolet iS50 (Thermo Scientific) using a diamond crystal attenuated total reflectance (ATR) unit.
8 Water content of the ILs were confirmed to be <1000 ppm by a coulometric Karl Fischer titrator
9 (Metrohm; 889D). Viscosity of the IL was measured with a viscometer (RheoSense; microVisc)
10 equipped with microchannel chips (Rheosense A05, A10, and B20). The phase transition of PIL-IL
11 gels was performed with a DSC (Mettler Toledo DSC3), where the PIL-IL gels (~15 mg) were pre-
12 loaded into Al pans and sealed in Ar atmosphere glovebox (VTI; H₂O and O₂ <0.1 ppm). The
13 sample pans were first held at 80 °C (5min), then cooled to -90 °C and held for 50 min, and finally
14 heated back to 80 °C with a rate of 10 °C/min under N₂ for three cycles. No differences were
15 observed among the cycles and therefore only the glass transition temperature (T_g) of the third
16 cycle is reported. The surface morphology and cross-sectional topography of the membranes
17 were taken by field emission scanning electron microscopy (FESEM; ThermoFisher Apreo 2S). All
18 membrane samples were sputtered with about 5 nm Pd prior to analysis for high conductivity
19 and better image resolution.

20

21 **CO₂ Binding Capacity**

22 The CO₂/N₂/O₂ gas mixture was prepared by mixing the CO₂ with the as-purchased synthetic air
23 (N₂/O₂) by mass flow controllers (MFCs; Brooks 5850i) with Labview® via data acquisition units
24 (DAQ; National Instrument 782604-01). The humidity control was achieved by a water bubbler.
25 For the precise control of temperature, the gas lines, including the water bubbler, was kept inside
26 an incubator (HettCube 400R; Across International LLC). The mixing of the gases for the desired
27 compositions of 410, 1000, 2500, 5000, 10000, and 20000 ppm of CO₂ at 22 °C and 40 % relative
28 humidity level (40 % RH at 22 °C refers to 7.9 Torr or 10.6 mbar) was done in a 300 mL metal
29 chamber (Swagelok) within the incubator. The gas flow rate was measured by ADM 2000

1 Flowmeter (J&W Scientific Inc., acquired by Agilent). A CO₂ analyzer (SBA-5, PPSystems Inc.) with
2 a detection range of 0 to 20,000 ppm was used to confirm the CO₂ concentration in the prepared
3 gas mixtures. To determine the CO₂ absorption capacity of the IL, the gas mixture with the set
4 CO₂ content (200 ml/min) was contacted with the IL (1 g) under 60 rpm agitation in a glass vial
5 (20 ml) for at least 6 h at 22 °C for equilibrium. The equilibrium for CO₂ saturation was reached
6 within 2-3 hr, whereas the equilibrium for the set relative humidity took longer. Therefore, a wait
7 time of 6 h was allowed to ensure the system reached thermodynamic equilibrium. The binding
8 capacity between CO₂ and IL carrier was studied by quantitative ¹³C-NMR. Following CO₂
9 absorption, 20 mg of the IL was sampled into 0.6 ml of 0.1 M Cr(ACAC)₃ DMSO-d₆ solvent and
10 quantification of the CO₂-IL complex followed the previously reported method.⁵⁸ The identified
11 products were identical to our previous report⁵⁸; briefly the peaks at 146, 154, and 158 ppm were
12 assigned to carbamate, carboxylate, and bicarbonate complexes.

13

14 **Self-Ion Diffusivities**

15 Self-diffusion coefficient of the IL sorbents was measured by Diffusion-Ordered Spectroscopy
16 (DOSY) on the same 500 MHz NMR. About 0.3 ml of DMSO-d₆ was loaded into the inner cell and
17 the top was flame sealed (or sealed with epoxy resin). About 1.5 ml of the CO₂-saturated IL (at
18 410, 1000, 2500, 5000, 10000, and 20000 ppm CO₂ under 40% RH) was transferred into the outer
19 cell and the atmosphere in the headspace was purged with the same atmosphere used for CO₂
20 absorption. The inner cell was then inserted into the outer cell and sealed with coded close cap
21 and parafilm to ensure a gas tight environment. The samples were measured using bipolar
22 gradient pulse sequence (ledbpg2s) and the Z-gradient diffusion probe (**Figure S3a**). The diffusion
23 times (Δ) and gradient pulse duration (δ) were optimized in subsequent experiments according
24 to practical needs, until full exponential decay pattern of magnetization was observed within 16
25 pulse gradient strengths (from 2 % to 98 %) (**Figure S3b** and **Figure S4a**). The isotopic self-
26 diffusivity (D) of ions was calculated using **equation 1** via MestReNova.

$$27 \quad M(g) = M_0 e^{[-(\gamma g \delta)^2 D (\Delta - \frac{\delta}{3})]} \quad (1)$$

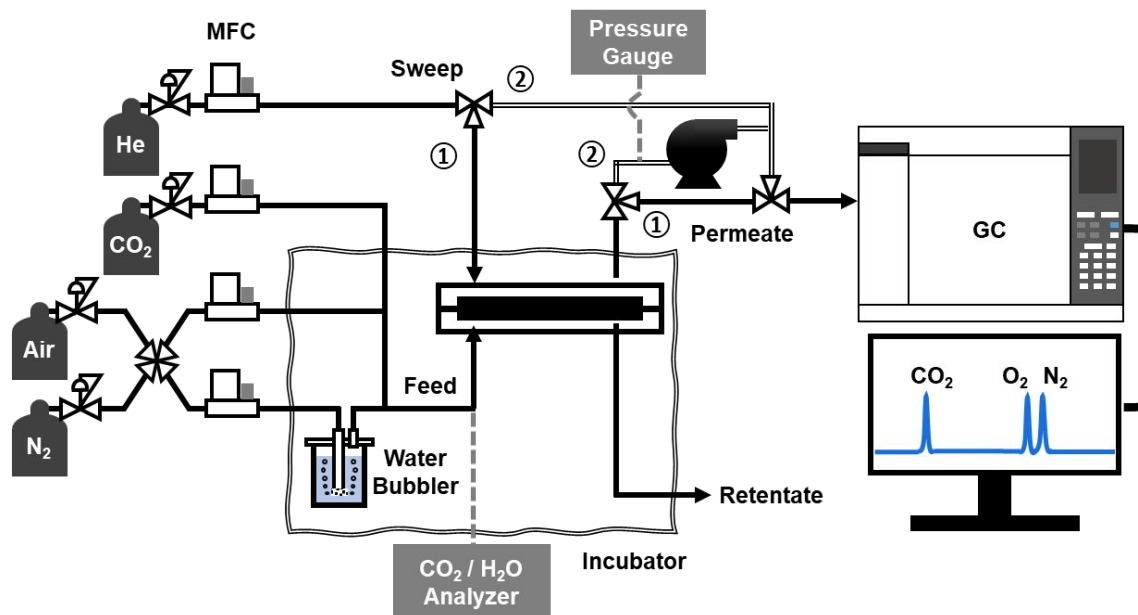
28 where γ is the gyromagnetic ratio, g is the magnitude of the gradient pulse, δ is the duration of
29 the gradient pulse, and Δ is the interval (drifting or diffusion time) between two gradient pulses

1 in the opposite direction. M_0 is the strength of magnetization without pulse field gradient
2 applied, whereas $M(g)$ is the measured magnetization that exponentially decay as a function of
3 applied pulse field gradient strength. An example of the calculated ^1H -DOSY is shown in **Figure**
4 **S4b**.

6 **Membrane Tests**

7 The gas separation performance of the PIL-IL/GO composite membrane was tested under both
8 sweep and vacuum modes. The membrane was placed in between two aluminum foils and
9 fastened in a stainless-steel permeation cell (Advantec). The membrane module along with the
10 bubbler and gas mixing chamber were kept within the temperature and humidity-controlled
11 incubator (HettCube 400R; Across International LLC). Simulated $\text{CO}_2/\text{N}_2/\text{O}_2/\text{H}_2\text{O}$ feed gas of 410,
12 1000, 2500, 5000, and 10,000 ppm CO_2 with various humidity level were prepared by fine tuning
13 the gas flow rate of the anhydrous CO_2 , anhydrous synthetic air ($\text{N}_2/\text{O}_2=80/20$), and moisture
14 saturation by passing the specific gas streams through the water bubbler. The $\text{CO}_2/\text{N}_2/\text{H}_2\text{O}$ feed
15 gas were prepared by mixing anhydrous CO_2 , anhydrous N_2 , and moisture saturated N_2 . **Figure 1**
16 shows the schematic of the membrane testing setup. The permeate side of the membrane
17 module has both the helium sweep (0 Torr gauge pressure; single solid line) and the vacuum (-
18 760 Torr gauge pressure; double solid line) capability for testing of different transmembrane
19 pressures. The flow rate of feed gas and sweep gas were kept constant as $200 \text{ cm}^3/\text{min}$. For tests
20 under the sweeping mode (labeled with pathway ① in **Figure 1**), the permeate gas was carried
21 by the He sweep directly to a gas chromatography, GC (Agilent 7890B) with a micro-packed
22 column and thermal conductivity detector (TCD) with He mobile phase for quantitative
23 compositional analysis. For tests under vacuum operation (labeled with pathway ② in **Figure 1**),
24 the permeate was first collected by a pump (Agilent; IDP-7 dry scroll pump) under vacuum and
25 then mixed with the He sweep, as shown, for GC analysis. The specific testing conditions are listed
26 in **Table 1**.

27



1
 2 **Figure 1.** Schematics of the membrane test unit. Permeate gas was collected and send to gas
 3 chromatogram (GC) either by He sweep (path ①) or by vacuum (path ②) for a transmembrane
 4 pressure of 0 or 1 atm, respectively. The balance gas of CO₂ is either synthetic air (N₂/O₂=80/20)
 5 or N₂ for the CO₂/N₂/O₂/H₂O or CO₂/N₂/H₂O mixtures, respectively.

6

7 **Table 1:** Fabricated FTM specifications and the membrane testing conditions

Membrane Substrate					
Membrane #	i	ii	iii	iv	v
Substrate	UF	bPES / PET			
Membrane area	5 cm ²				
Selective Layer					
PIL – IL / GO (mg)	0.2 – 20 / 0.2		0.4 – 40 / 0.4	0.5 – 50 / 0.5	1.25 – 3.75 / 1
Thickness (μm)	0.9		1.4	1.6	2.0
Membrane Testing Condition					
Feed; Sweep	200 cm ³ /min; 200 cm ³ /min				
CO ₂ in feed (ppm)	410, 2500, and 10000 (1 %) CO ₂ balanced with N ₂ or synthetic air (N ₂ /O ₂ =80/20) at 760 Torr				

Transmembrane Pressure (ΔP ; Torr)	0	760
Temperature (K)	295 and 313 K	
Relative Humidity (% RH)	0, 40, and 80	40

1

2

3 The gas separation performance was calculated in gas permeance unit (GPU; 1 GPU = 3.348×10^{-10} mol m⁻² s⁻¹ Pa⁻¹) by **equation 2**.

$$4 \quad P_i = 10^6 (Q_i / (A \cdot \Delta p_i)) \quad (2)$$

6 where Q_i is the permeating rate of component i (cm³/s), A is the membrane area (5.06 cm²), and
 7 Δp_i is the transmembrane partial pressure gradient for component i (cmHg). The uncertainty in
 8 permeance (P_i) was determined from the propagation of error analysis using the respective
 9 uncertainties in A (± 0.11 cm² based on the measured membrane coupon radius of ± 0.2 mm), Δ
 10 p_i (± 0.01 cmHg based on the measured concentrations by GC) and the standard deviation in the
 11 repeated measurements for Q_i (varied for each of the conditions in the range of 0.0001 – 0.0003
 12 cm³/s for 5 measurements).

13

14 The selectivity of CO₂ over N₂ (α_{CO_2/N_2}) and CO₂ over O₂ (α_{CO_2/O_2}) are calculated using **equation**
 15 **3** and **equation 4**, respectively. The separation ratio ($\alpha_{CO_2/(N_2 + O_2)}$), which is the permeance ratio
 16 of CO₂ over the sum of N₂ and O₂, is a parameter that better describes the performance of gas
 17 separation in ternary gas mixtures, and it is calculated using **equation 5**.

$$18 \quad \alpha_{CO_2/N_2} = \frac{P_{CO_2}}{P_{N_2}} \quad (3)$$

$$19 \quad \alpha_{CO_2/O_2} = \frac{P_{CO_2}}{P_{O_2}} \quad (4)$$

$$20 \quad \alpha_{CO_2/(N_2 + O_2)} = \frac{P_{CO_2}}{P_{N_2} + P_{O_2}} \quad (5)$$

21

1 The dependence of CO₂ permeance on the CO₂ partial pressure of the feed is described by a
 2 homogenous reactive diffusion model given in **equation 6**.^{39,47}

$$3 \quad \frac{P_{CO_2}}{l} = \frac{P_{CO_2}^0}{l} \left[1 + \eta_{CO_2} \left(\sqrt{1 + \frac{p_{CO_2}^*}{p_{CO_2}^h}} - 1 \right) \right] \quad (6)$$

4 where l is the thickness of the membrane, P_{CO_2}/l is the measured CO₂ permeance, $P_{CO_2}^0/l$ is a fit
 5 parameter that represent the CO₂ permeance (GPU) at saturation of carriers (corresponding to
 6 the CO₂ permeance from S-D pathway), η_{CO_2} is the efficacy of the facilitated transport pathway,
 7 $p_{CO_2}^*$ is the partial pressure of CO₂ in the feed when the carriers are saturated with CO₂, and $p_{CO_2}^h$ is
 8 the set CO₂ partial pressure in the feed.

1 RESULTS AND DISCUSSION

2 We first present the results from the characterization of the CO₂ carrier, namely the [EMIM][2-
3 CNpyr], in terms of its CO₂ binding capacity in the presence of N₂ and O₂, ion self-diffusivities, and
4 the thermal behavior when gelled with PIL. The fabricated membranes with the PIL-IL gel is then
5 described through their topological and cross-sectional features determined by SEM as well as
6 the specific interactions among the PIL, IL, and GO components examined by FTIR and NMR
7 methods. Finally, the CO₂ separation performance of the FTMs under synthetic air feed and at
8 varying temperature and humidity conditions are presented.

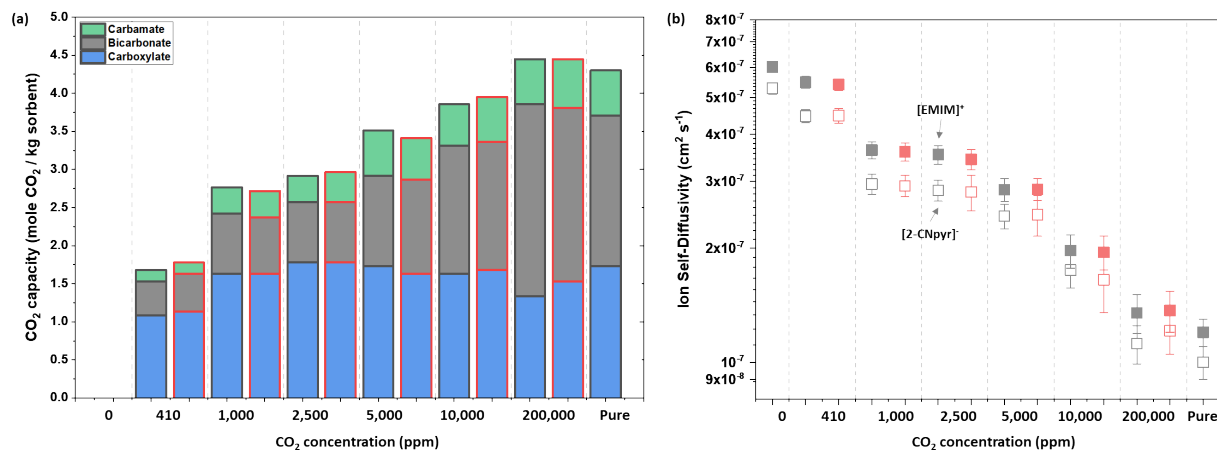
9

10 CO₂ binding and transport

11 CO₂ binding to the IL and the ion diffusivities in the presence of O₂ (16-20 %) is studied at 22 °C
12 and 40% RH (10.6 mbar). The CO₂ absorption by [EMIM][2-CNpyr] has been previously shown^{56,58}
13 to form carbamate (CO₂ binding to the pyrrole anion), carboxylate (CO₂ binding to the
14 imidazolium cation), and bicarbonate (CO₂ binding to the co-absorbed water) species in both
15 pure CO₂ and CO₂/N₂. The distribution of these products was found to be different at low CO₂
16 partial pressures in N₂ compared to pure CO₂. **Figure 2a** shows the breakdown of the measured
17 CO₂ binding capacities, calculated from the ¹³C-NMR peak integration of *carbamate* at 146 ppm
18 (-N-COO), *carboxylate* at 154 ppm), and *bicarbonate* (HO-COO) with (red bordered) and without
19 O₂ presence (black bordered). At 410 ppm, 40 % of the total capacity under pure CO₂ is achieved
20 in both cases of with and without O₂, showing the strong interactions between the IL and CO₂.
21 The capacity at 2500 ppm of CO₂ is about 60 % of the total capacity under pure CO₂ (4.3 mole
22 CO₂/kg sorbent). Within the gas compositions studied, there is no significant influence of O₂ on
23 the measured capacity of CO₂. The physisorbed of CO₂ within the entropic voids of the [EMIM][2-
24 CNpyr] is expected to be less than 3 % of the overall CO₂ capacity⁵⁹, whereas the physisorbed of
25 O₂ is expected to be at least a factor lower⁶⁰ than that of physisorbed CO₂ in ILs in general. This
26 is due to the high polarizability of the quadrupolar CO₂ within ionic environments, in contrast to
27 nonpolar O₂. The measured bulk viscosity of the IL is also not influenced much with O₂ (**Figure**
28 **S5a**). However, as seen in **Figure 2b**, the measured ideal diffusivities of the imidazolium (filled

1 symbols) and the pyrrole (hollow symbols) demonstrate a weak dependence on O_2 (3-5%
 2 difference between gray and red symbols) and a strong dependence on CO_2 .

3



4

5 **Figure 2.** (a) Measured CO₂ capacity of [EMIM][2-CNpyr] at 22 °C and 40% RH (10.6 mbar) by
 6 quantitative ¹³C-NMR with and without (red bordered bars) O₂ in the synthetic air feed. The O₂
 7 concentration in the gas mixtures was maintained at about 20 % with the exception of 200,000
 8 ppm CO₂ where O₂ concentration was 16 %. The uncertainty of the breakdown capacity is
 9 calculated from the signal to noise ratio to be less than 0.05 mole CO₂/kg sorbent. (b) The
 10 dependence of self-diffusivities of [EMIM]⁺ (filled symbol) and [2-CNpyr]⁻ (hollow symbol) on
 11 the CO₂ concentration in the absorbed feed gas with (red) and without (gray) O₂.

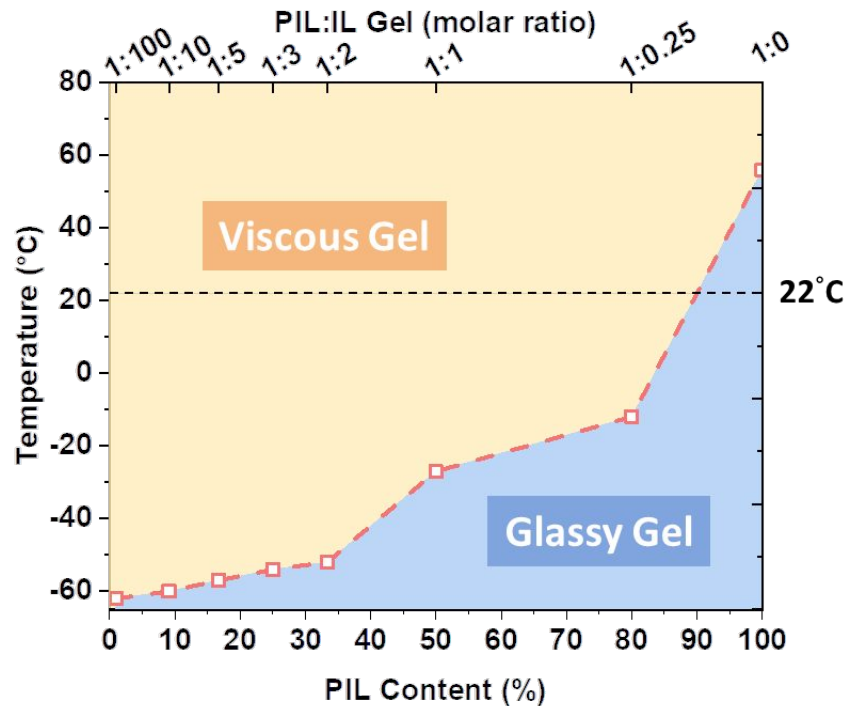
12

13 The ion self-diffusivities were measured by ¹H-DOSY NMR (**Figure S4**). The diffusivity of
 14 imidazolium (D⁺) is higher than the pyrrole (D⁻) despite the smaller size of anion. Previous
 15 studies^{61,62} on various ILs reported similar observations and attributed this trend to the hydrogen
 16 bonding associated mostly with the anions. The diffusivity of [EMIM], [2-CNpyr], and their CO₂-
 17 complexes are around 10⁻⁷ cm²/s at 22 °C, which is an order of magnitude higher than the
 18 reported ion diffusivities for a similar CO₂ reactive IL 1-methyl-3-ethylimidazolium acetate (~10⁻⁸
 19 cm²/s with a viscosity of 2700 cP)⁶³. The CO₂-complexed ions could not be resolved effectively
 20 from their parent ions as they appeared as single peak for both the imidazolium and the pyrrole.
 21 This is attributed to the strong H-bonding⁵⁸ between the CO₂ complexed and un-complexed ions
 22 and the fast exchange of proton between these species. The strong dependence of the ideal

1 diffusivity of both the cation (D^+) and the anion (D^-) on the quantity of CO_2 within the IL is also
2 indicative of the increased intermolecular hydrogen bonding that leads to slower diffusion. It
3 should be noted that the direct deconvolution of different transport mechanism of CO_2 (diffusion,
4 hopping, and vehicular motion) is not possible at this point by ^1H -DOSY since CO_2 itself is not
5 proton-bearing. Therefore, the measured diffusivities of ions reflect the overall transport of
6 carrier- CO_2 complex. The (D^+/D^-) ratio remained in the range of 1.18-1.23 for all of the conditions
7 studied, suggesting no major changes in the solvation environment when O_2 is present in the
8 carrier liquid.

9
10 The incorporation of PIL into IL provides mechanical reinforcement by forming a non-crosslinked
11 gel. In turn, the IL component acts as the plasticizer for mobility enhancement of the CO_2 carrier.
12 **Figure 3** shows the phase-transition of PIL-IL gels in the bulk as characterized by DSC. The plotted
13 red squares are the glass transition temperatures (T_g) of the PIL-IL gels, as determined from the
14 midpoint of the transition region of the DSC curves. The T_g decreases as the amount of PIL
15 decreases. In order to have a mobile carrier within the membrane at cabin or atmospheric
16 temperatures, it is more desirable to have a viscous gel than a glassy one. Therefore, optimization
17 of the PIL-IL content is necessary for a targeted permeance. Too high of a PIL content would
18 increase the membrane resistance while too high of an IL content may not demonstrate enough
19 mechanical stability against large transmembrane pressures. We tested the 1:100 PIL:IL
20 composition, similar to our previous work⁵⁶ to allow for high carrier mobility, for the sweeping
21 mode of operation and the 1:3 PIL:IL composition to improve stability of the carrier within the
22 membrane architecture against vacuum mode of operation on the permeate side.

23



1
 2 **Figure 3.** The phase diagram of PIL:IL mixture (in molar ratio) measured by DSC, with a scanning
 3 rate of 10 °C/min under N₂. The glass transition (T_g) points are connected with red dashed line as
 4 the hypothetical trend of phase-transition of the gel from the glassy state to elastomeric state.
 5 The plot of DSC curve from which T_g was obtained is given in **Figure S6**.

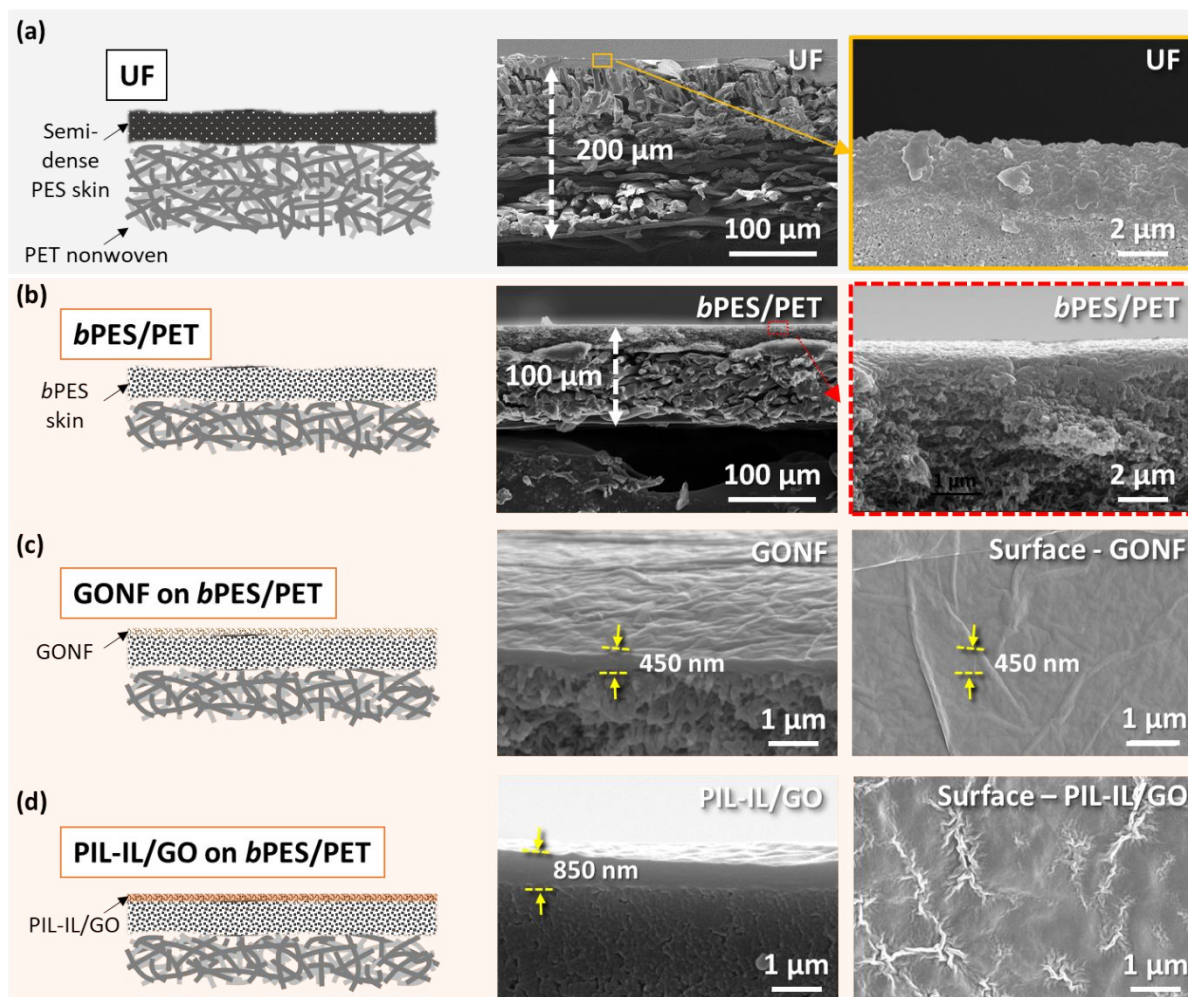
6

7 **Characterization of PIL-IL/GO membrane**

8 In comparison to the commercial UF membrane substrate (**Figure 3a**), the schematics and the
 9 SEM images of *b*PES/PET substrate are shown in **Figure 3b**. The *b*PES skin layer has an
 10 interconnected porous structure with a pore size of roughly 30-40 nm⁶⁴ (**Figure 3b** right panel)
 11 whereas the UF substrate has a semi-dense PES skin layer (**Figure 3a** right panel). The fabrication
 12 of GONF on the *b*PES/PET substrate was done by vacuum filtering where the GO nanosheets
 13 (each with about 0.3 μ width) were deposited homogeneously to give a wrinkled top surface
 14 (**Figure 3c** right panel). The deposited GONF is estimated to consist of about 250 to 260 GO layers,
 15 based on the individual sheet thickness of 0.8 nm and spacing of 1 nm in between the GO layers.⁵⁶
 16 The impregnation of the PIL-IL gel into the GONF layer caused swelling and change in surface

1 morphology with a final PIL-IL/GO selective layer thickness of about 850 nm (**Figure 3d**) in
 2 comparison to GONF thickness of about 450 nm (**Figure 3c**).

3



4

5 **Figure 4.** Schematics and the cross-sectional SEM images of UF substrate (a), the fabricated
 6 *bPES/PET* substrate (b), GONF on *bPES/PET* substrate (c), and PIL-IL/GO selective layer on
 7 *bPES/PET* substrate (d). The zoomed-in images on the right for a and b panels show the difference
 8 in porosity of the PES skin layer. The surface morphology shown on the right of panels c and d
 9 represent the GONF top surface before and after impregnation with PIL-IL gel, respectively. The
 10 surface morphology of the unmodified UF and *bPES/PET* substrates are shown in **Figure S7a**.

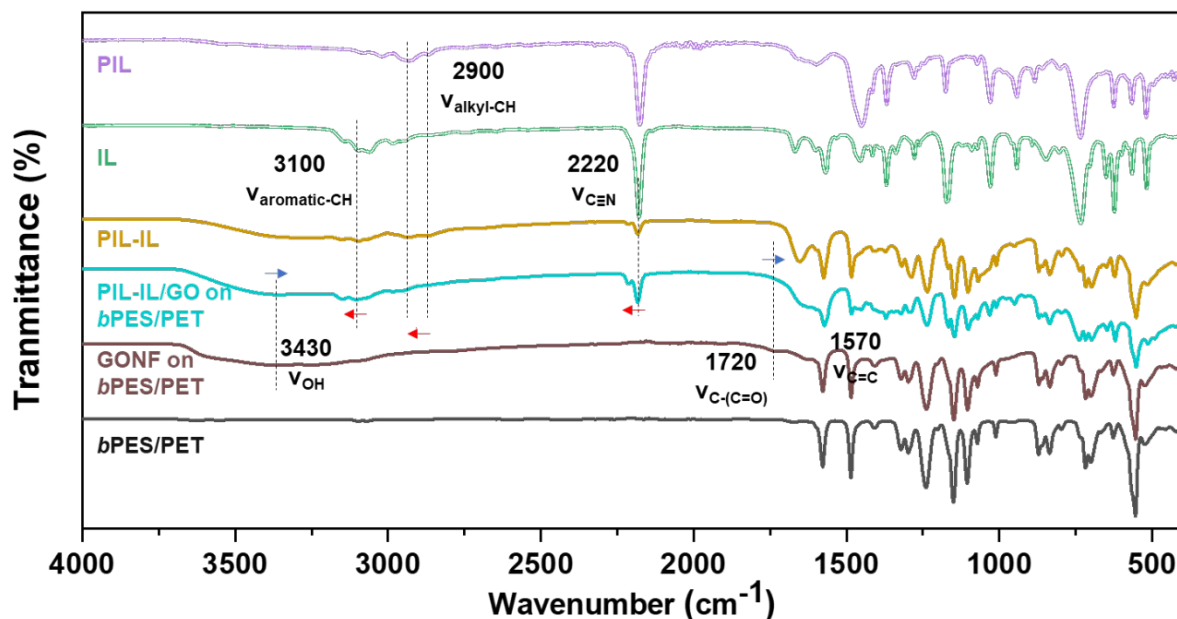
11

12 The specific interactions between GO and PIL-IL gel were probed by FTIR and NMR methods.

13 **Figure 5** shows the FTIR spectra of PIL-IL/GO on *bPES/PET* substrate (ii in **Table 1**), where the

1 characteristic features of PIL-IL ($\nu_{\text{aromatic-CH}}$ 3100 cm^{-1} , $\nu_{\text{alkyl-CH}}$ 2900 cm^{-1} , and $\nu_{\text{C}\equiv\text{N}}$ 2220 cm^{-1}) and
 2 GO (ν_{OH} 3430 cm^{-1} , $\nu_{\text{C}=\text{O}}$ 1720 cm^{-1} , and $\nu_{\text{C}=\text{C}}$ 1570 cm^{-1}) were confirmed. The observation of
 3 the red-shifted GO peaks (ν_{OH} 3430 cm^{-1} and $\nu_{\text{C}=\text{O}}$ 1720 cm^{-1} ; highlighted with red arrows) and
 4 the blue-shifted PIL-IL peaks ($\nu_{\text{aromatic-CH}}$ 3100 cm^{-1} , $\nu_{\text{alkyl-CH}}$ 2900 cm^{-1} , and $\nu_{\text{C}\equiv\text{N}}$ 2220 cm^{-1} ;
 5 highlighted with blue arrows) suggest the molecular interactions between the PIL, IL, and GO
 6 components.⁶⁵ **Figure S7b** compares the peak shifts of the PIL-IL/GO on UF and *b*PES/PET
 7 substrate, in which we don't see much difference in the featured characteristic peaks. Therefore,
 8 we concluded that the nano-confinement of PIL-IL in GONF is effective, and the PIL-IL gel is not
 9 leached out into the substrate even when the pore size increase from UF (3-4 nm) to *b*PES/PET
 10 (30-40 nm). The photo images of the PIL-IL/GO and GONF on UF and *b*PES/PET substrates are in
 11 **Figure S7a**.

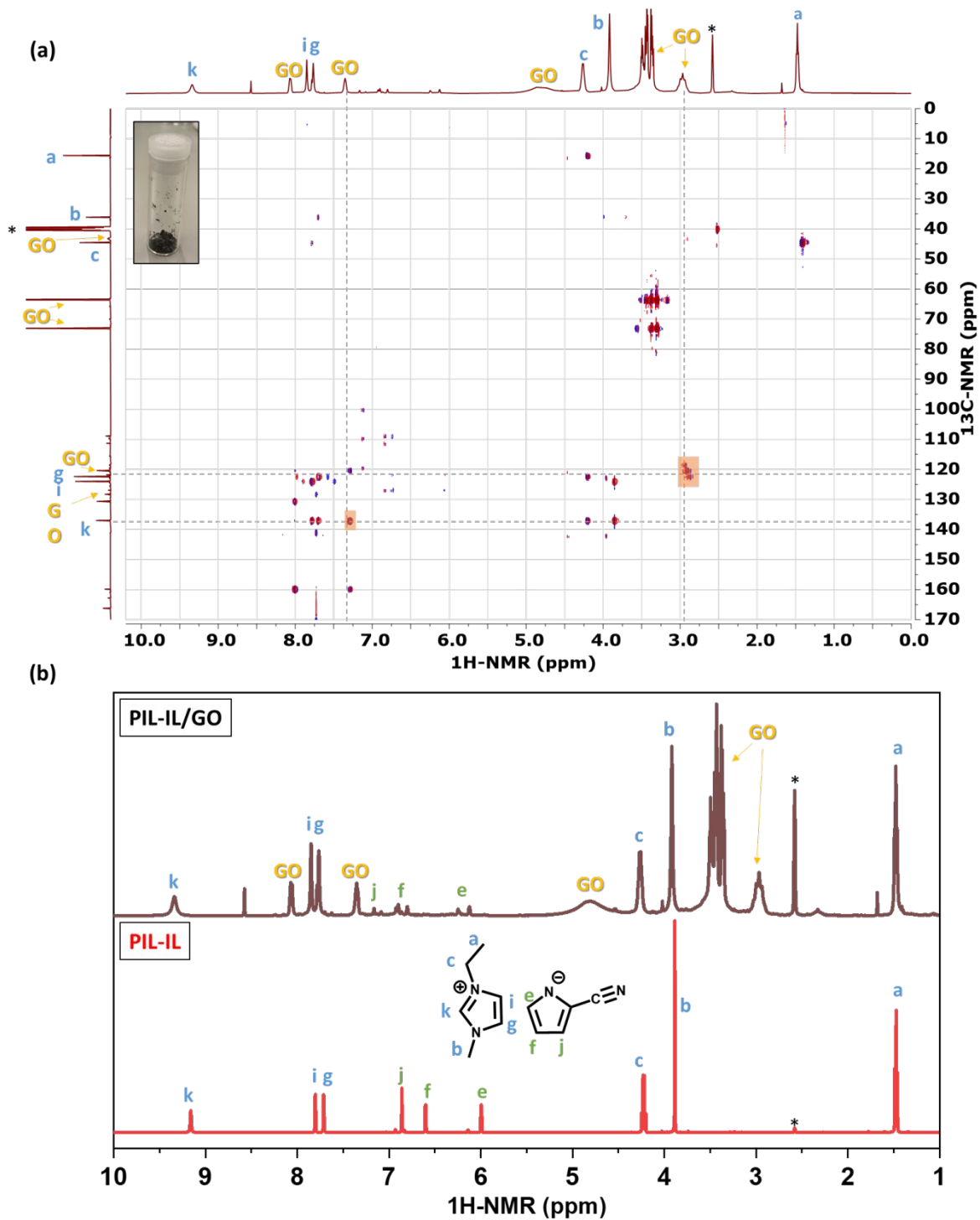
12



13

14 **Figure 5.** FTIR spectra of PIL, IL, PIL-IL, PIL-IL/GO on *b*PES/PET, GONF on *b*PES/PET, and *b*PES/PET
 15 substrate. The vertical dashed lines, from high to low wavenumber, mark the resonance peak of
 16 ν_{OH} 3430 cm^{-1} (GONF), $\nu_{\text{aromatic-CH}}$ 3100 cm^{-1} (IL), $\nu_{\text{alkyl-CH}}$ 2900 cm^{-1} (PIL), $\nu_{\text{C}\equiv\text{N}}$ 2220 cm^{-1} (PIL and
 17 IL), $\nu_{\text{C}=\text{O}}$ 1720 cm^{-1} (GONF), $\nu_{\text{C}=\text{C}}$ 1570 cm^{-1} (GONF). The arrows indicate the red and blue shift-
 18 direction of each vibration in the PIL-IL/GO, due to molecular interactions among the
 19 constituents.

1
2 The HMBC NMR (**Figure 6a**) further provided support to the interactions observed between the
3 PIL-IL and GO by FTIR by specifically probing the correlated ^1H and ^{13}C within the selective layer
4 components. In order to remove the interference from the majority component, which is the
5 substrate, the PIL-IL/GO flakes (**Figure 6a** inset) were scraped from the membrane surface and
6 re-dissolved in DMSO-d_6 for HMBC. The correlations between the imidazolium ring (g, i, and k)
7 and GO were highlighted in yellow at the intersections of the dashed lines (**Figure 6a**). This
8 interaction between $[\text{EMIM}]^+$ and GO is ascribed to both the π - π and electrostatic interactions.⁶⁵⁻
9 ⁶⁷ Moreover, $^1\text{H-NMR}$ of PIL-IL/GO also suggests the interaction between PIL-IL and GONF. **Figure**
10 **6b** compares the $^1\text{H-NMR}$ of PIL-IL/GO and PIL-IL gel. With a molar ratio of PIL:IL = 1:100, we
11 observed the spectra to be almost the same as IL (**Figure S1a**) since the proton signal of PIL is
12 diminished due to its low concentration (**Figure 6b** bottom). With the confinement of PIL-IL
13 within the GONF, the characteristic peaks of $[\text{EMIM}]^+$ cation “a, b, c, g, i, and k” broaden⁶⁸ due to
14 the relatively slow movement of the ions within the NMR time scale (**Figure 6b** top). Such
15 broadening effect was observed only in the IL constituent and was not observed on the line width
16 of the d-solvent (DMSO-d_6 at 2.58 ppm, labeled with *). The OH moiety of GO component is also
17 downshifted to 4.7 ppm (**Figure 6b** top) from 3.4 ppm that is seen in pure GO sample without the
18 presence of PIL or IL (**Figure S8**). This shift further supports the existence of interactions between
19 the PIL-IL and GO.
20
21



1
 2 **Figure 6.** (a) HMBC spectra showing the molecular interactions between PIL, IL, and GO
 3 components. Inset shows the images of PIL-IL/GO material collected by scraping off the top
 4 selective layer from the PIL-IL/GO on *b*PES/PET to redisperse in DMSO- d_6 for HMBC NMR. (b) ^1H -
 5 NMR of the PIL-IL/GO and PIL-IL gel. The GO peaks, from high field to down field, are likely due

1 to the native alkyl-CH (~3 ppm), OH (4.7 ppm), aromatic-CH (~7 ppm) functionalities that are
2 captured due to their interaction with the IL. The NMR of pure GO is shown in **Figure S8**.

3

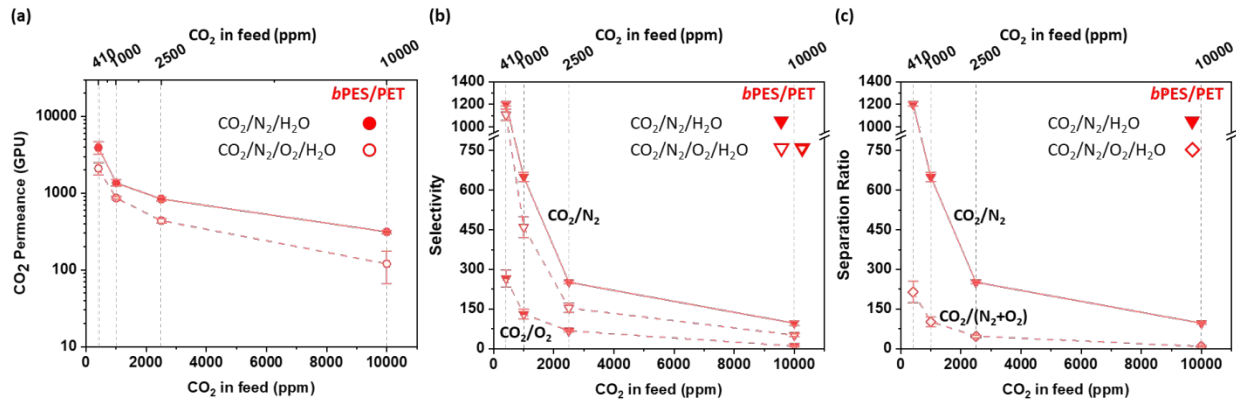
4 **CO₂ Separation**

5 The CO₂ permeance and CO₂ selectivity against N₂ and O₂ with the PIL-IL/GO FTMs were
6 measured by membrane testing according to the conditions summarized in **Table 1**. **Figure 7**
7 shows the performance of PIL-IL/GO on *b*PES/PET substrate (**ii** in **Table 1**); both with (hollowed
8 symbols) and without O₂ (filled symbols). CO₂ permeance of 3900 GPU (**Figure 7a**) and CO₂/N₂
9 selectivity of 1200 (**Figure 7b**) were measured under 410 ppm CO₂ with CO₂/N₂/H₂O mixture feed
10 at 40% RH and 22 °C. Under 2500 ppm CO₂ (cabin air), the performance was 1360 GPU with a
11 CO₂/N₂ selectivity of 650. The exponential decrease in CO₂ permeance with increased CO₂
12 concentration in feed is a characteristic trait of facilitated transport (F-T) mechanism. The
13 permeances for the non-reactive O₂ and N₂ stay constant around 6 GPU for O₂ and 1 GPU for N₂.
14 The F-T pathway dominates over S-D mechanism for CO₂ transport at these low partial pressure
15 conditions. While the CO₂/N₂ selectivity of the FTM with *b*PES/PET substrate (**ii** in **Table 1**) was
16 about the same as the one with the UF substrate (**i** in **Table 1**; **Figure S9b**), PIL-IL/GO on *b*PES/PET
17 presented 10 % higher CO₂ permeance under both DAC and cabin air conditions with CO₂/N₂/H₂O
18 mixture feed (**Figure S9a**). Following the resistance-in-series model, this increase in permeance
19 is ascribed to the thinner *b*PES skin layer with larger pore size (30-40 nm) that is interconnected
20 as opposed to the semi-dense PES layer (pore size 3-4 nm) of the commercial UF substrate.^{57,64,69}
21 The CO₂ permeance decreased by about 45% in the presence of O₂ to 2100 GPU at 410 ppm of
22 CO₂ (**Figure 7a**). This was observed irrespective of the substrate used (**Figure S9a**). Recalling that
23 the solubility of CO₂ in IL is barely changed with and without the presence of O₂ presence (**Figure**
24 **2a**), we suggest that the decrease in CO₂ permeance is related with the slower diffusion of CO₂
25 and CO₂-complexes within the membrane (**Figure 2b**). The CO₂/O₂ selectivity (265 at 410 ppm
26 CO₂) is lower than that of CO₂/N₂ selectivity (1100) since O₂ (~ 5 GPU) is in general more
27 permeable than N₂ (~1.5 GPU), mainly due to their difference in molecular size (O₂: 3.46 Å vs. N₂:
28 3.64 Å). **Figure 7c** shows the separation ratio of PIL-IL/GO on *b*PES/PET with and without O₂. The

1 PIL-IL/GO on *b*PES/PET was observed to have lower separation ratio due to the higher permeance
 2 of O₂ than N₂.

3

4



5

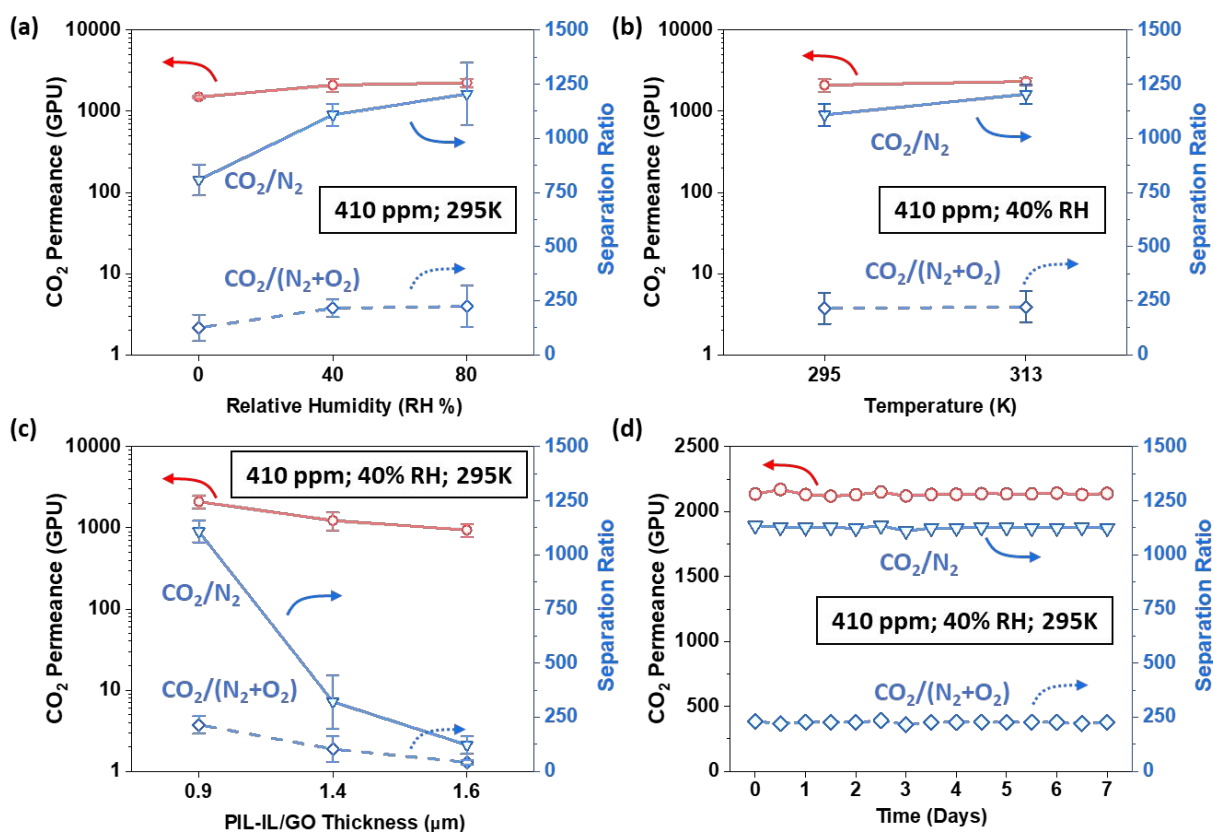
6 **Figure 7.** (a) Permeance of PIL-IL/GO on *b*PES/PET (i in **Table 1**) under CO₂/N₂/H₂O (filled circle)
 7 and CO₂/N₂/O₂/H₂O (hollowed circle). (b) CO₂/N₂ and CO₂/O₂ selectivities. (c) CO₂/(N₂+O₂)
 8 separation ratio. Notice that for CO₂/N₂/H₂O feed, the CO₂/(N₂+O₂) separation ratio is the same
 9 as CO₂/N₂ selectivity. The feed gas had a humidity level of 40% RH at 22 °C; 10.6 mbar moisture.

10

11 The experimental data presented in **Figure 7a** was fitted to the facilitated transport model
 12 (**equation 6**) to extract parameters of $P_{CO_2}^0/l$ and $p_{CO_2}^*$ (**Figure S10**). The $P_{CO_2}^0/l$ parameter (in units
 13 of GPU) corresponds to the CO₂ permeance of FTMs at complete carrier saturation and
 14 therefore represents the S-D portion of the overall CO₂ permeance. The fitted values of $P_{CO_2}^0/l$
 15 are magnitudes lower than the overall measured CO₂ permeance P_{CO_2}/l ; consistent with FTM
 16 behavior where CO₂ permeance decreases with increasing CO₂ concentration since the
 17 membrane starts to behave more like S-D membrane or even membrane absorbers at high CO₂
 18 partial pressures. The extracted CO₂ permeance at carrier saturation of the PIL-IL/GO on UF
 19 under CO₂/N₂ is 32.6 GPU, which is in the vicinity of the previously reported CO₂ permeance of
 20 19 GPU at higher CO₂ concentration of 15 % at 22 °C.⁵⁶ Further comparing the extracted value of
 21 $p_{CO_2}^*$ (**Figure S10** inset table) under the condition with and without O₂, CO₂ saturation of carriers
 22 within membrane seems more likely to happen when there is O₂ presence, regardless of the

1 membrane substrate used. The slower ion-self diffusivity measured in **Figure 2b** when there is O₂
2 also supports this observation.

3
4 Factors like humidity⁷⁰ and temperature³⁹ are known to influence the transport behavior in FTM.
5 Under high humidity, water is co-absorbed with CO₂. The presence of water is known to decrease
6 the viscosity of ILs and it also increases the CO₂ capacity due to the reaction between CO₂ and
7 water that forms bicarbonate⁵⁶. On the other hand, increase in temperature not only increases
8 chain mobility in PIL (hence faster CO₂ transport) but also encourages the dissociation of IL-CO₂
9 complex (hence faster CO₂ release) due to the exothermic nature of CO₂ absorption. Therefore,
10 CO₂ separation from air for PIL-IL/GO on *b*PES/PET was evaluated at different humidity levels and
11 temperatures as shown in **Figure 8a** and **8b**, respectively. The CO₂ permeance, CO₂/N₂ selectivity,
12 and separation ratio all increase with increased humidity and temperature, primarily owing to
13 the faster transport of the CO₂. (See SI for more detailed discuss on the temperature effect on
14 FTM performance) A higher CO₂ transport was achieved with higher moisture content, since
15 humidity not only increases the binding of CO₂ to IL carrier (via greater extent of bicarbonate
16 formation) but also increases the diffusivity of the carriers due to lubrication effect from water
17 co-absorption (**Figure S11**). With increased temperature, CO₂ and IL-CO₂ complex diffusivities are
18 expected to increase, so does the dissociation rate of IL-CO₂ complex. There is much discussion
19 in the field⁷¹ on whether it is the increase of the carrier mobility⁴⁹ or the CO₂ dissociation rate⁴⁷
20 that dominates for higher CO₂ separation performance with increased temperature. A recent
21 study on high performance FTMs at room temperature suggest the rate determining step is the
22 diffusion⁵⁴. Therefore, not surprisingly the separation performance decayed with increased
23 thickness of selective layer (from ii to iv in **Table 1**) as seen in **Figure 8c** due to the increased film
24 resistance to diffusion. **Figure 8d** further demonstrates the stability of PIL-IL/GO on *b*PES/PET
25 over the course of 7 days under continuous feed of 410 ppm CO₂ at 40% RH and 295K. We believe
26 that the nano-confinements of PIL-IL within GO (through (1) π - π interaction and (2) electrostatic
27 interactions) played a pivotal role for this stability.⁵⁶

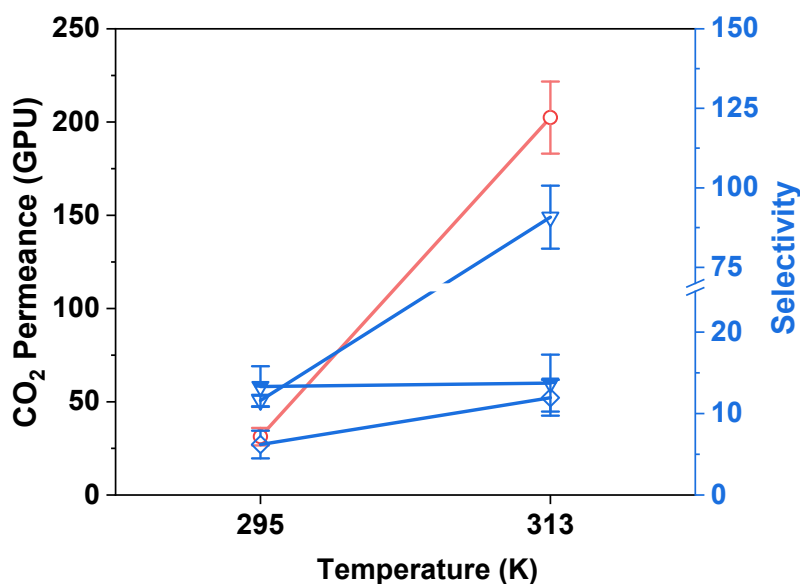


1
2 **Figure 8.** The change in CO₂ separation performance with humidity (a), temperature (b),
3 membrane thickness (c), and time (d). Membrane ii (in Table 1) is used in panel (a), (b), and (d);
4 and membrane ii, iii, and iv are used in panel (c).

5
6 We further tested PIL-IL/GO on *b*PES/PET under vacuum operation with 760 Torr transmembrane
7 pressure. Membranes ii, iii, and iv (in Table 1) leaked, as we noticed the transmembrane pressure
8 gradient could not be maintained and the permeate composition was almost the same as the
9 feed, suggesting the need of further mechanical reinforcement on the selective PIL-IL/GO layer.
10 **Table S1** shows our efforts of changing the PIL-IL/GO composition by gradually increasing the PIL
11 and GO loading of the selective layer. The increase of PIL and GO components increased the
12 mechanical stability of the PIL-IL/GO; however, this was accompanied with significant reductions
13 in CO₂ binding capacity and transport. The high content of PIL also led to a relative brittle film
14 (see **Figure 3**) results in cracks even under the plasticization by moisture at 40% RH (i.e., samples
15 3 and 7 in **Table S1**). It was demonstrated that a PIL-IL/GO of 1.27-3.75/1 (v in **Table 1**; sample

1 21 in **Table S1**) withstands the pressure gradient. **Figure 9** shows CO₂ separation performance at
2 295 and 313 K for the FTM sample **v**. At 295K, the F-T pathway appears to be more hindered due
3 to the higher PIL content, which is less reactive to CO₂ without the imidazolium moiety in the
4 ionomer structure, and the thicker selective layer. The performance resembles an S-D
5 membrane, where a CO₂ permeance of 31 GPU and separation ratio of 6.2 were measured. At
6 313 K, the F-T mechanism was enhanced due to improved diffusivity with increased temperature,
7 the CO₂ permeance increased by 15-fold along with an increase in CO₂/N₂ selectivity. However,
8 the CO₂/O₂ selectivity remains about the same, possibly due to the enhanced O₂ diffusion. These
9 results demonstrate that even a relatively small increase in the thickness of the selective layer
10 for mechanical stability results in dramatic reduction in the FTM performance, thus identifying
11 the mass transport resistance as the most critical factor. Therefore, our recommendation for
12 future research direction for PIL-IL type of FTMs is chemical modifications of the selective layer
13 so that the carriers can be covalently bonded in order to achieve both the superior separation
14 performance and the durability in particular for transmembrane pressures larger than zero.

15



16

17 **Figure 9.** Performance of vacuum operation of PIL-IL/GO on *bPES/PET* (**v** in **Table 1**) under 410
18 ppm CO₂ with ternary mixture at 22 and 40 °C; both with 40% RH.

19

20

1 CONCLUSIONS

2 An FTM with PIL-IL/GO selective layer was fabricated using a highly permeable bicontinuous
3 structured *b*PES/PET substrate. The nanoconfinement of PIL-IL within the GONF layer through
4 ionic interactions between the carriers and the GO flakes and π - π interactions between the
5 aromatic moieties were effective in maintaining the membrane stability under zero
6 transmembrane pressure. The presence of O₂ in the feed did not affect the carrier-CO₂ binding
7 capacity, however it resulted in slightly slower CO₂ transport. The fabricated FTM with PIL-IL/GO
8 selective layer and the *b*PES/PET substrate presented a CO₂ permeance of 2100 GPU and high
9 selectivities of CO₂/N₂ (1100) and CO₂/O₂ (265) selectivity under conditions relevant to DAC (410
10 ppm CO₂, 40% RH, 295 K). Under 2500 ppm of CO₂, conditions relevant to cabin air, the
11 permeance decreases to 430 GPU while the CO₂/N₂ selectivity and CO₂/O₂ selectivity dropped to
12 150 and 67, respectively. These results demonstrate a superior performance, especially the
13 CO₂/O₂ selectivity, among the known FTMs reported to date. Further, this study represents the
14 first FTM for CO₂ separation from air. To improve the membrane stability and to prevent leaching
15 of the carrier for operations under a positive transmembrane pressure, the selective layer
16 thickness was increased. The thicker membranes presented significant resistance thus resulting
17 in lower separation performance. In order to further tune the membrane stability without
18 increasing the thickness and resistance, covalent interactions between the PIL-IL and GO within
19 a thin selective layer are determined to be necessary.

20

21 ASSOCIATED CONTENT

22 NMR characterization of IL, PIL, and GO; pulse sequence and the spectra recorded for ¹H-DOSY
23 NMR; viscosity and water content of IL as a function of CO₂ concentration and humidity; FTIR,
24 SEM, and photo images of the membranes; Details of the transport model fit; membrane
25 specifications for the tested vacuum operation.

26

27 AUTHOR INFORMATION

28 Corresponding Author

1 Burcu Gurkan - Department of Chemical Engineering Biomolecular Engineering, Case Western
2 Reserve University, Cleveland, Ohio 44106, United States; orcid.org/0000-0003-4886-3350;
3 Email: beg23@case.edu

4

5 **Authors**

6 Yun-Yang Lee – Department of Chemical Engineering Biomolecular Engineering, Case Western
7 Reserve University, Cleveland, Ohio 44106, United States; [orcid.org/ 0000-0002-4165-0857](https://orcid.org/0000-0002-4165-0857);
8 Email: yxl2286@case.edu

9

10 Nalinda P. Wickramasinghe – Northeast Ohio High Field NMR Facility, Case Western Reserve
11 University, Cleveland, Ohio 44106, United States; [orcid.org/ 0000-0002-8700-2775](https://orcid.org/0000-0002-8700-2775); Email:
12 npw8@case.edu

13

14 Ruth Dikki – Department of Chemical Engineering Biomolecular Engineering, Case Western
15 Reserve University, Cleveland, Ohio 44106, United States

16

17 Darrell L. Jan – Ames Research Center, National Aeronautics and Space Administration, Moffett
18 Field, California 94043, United States; Email: darrell.l.jan@nasa.gov

19

20 **AUTHOR CONTRIBUTIONS**

21 Y.Y.L. synthesized the IL and PIL, and fabricated, characterized and tested the membranes. N.P.W
22 assisted on performing the DOSY and HMBC NMR. R.D measured CO₂ capacities. D.L.J.
23 contributed to the experimental plans and the discussions on the CO₂ removal from cabin air. B.G
24 oversaw the experiments and analysis. All authors contributed to the writing of the manuscript.

25

26 **ACKNOWLEDGEMENTS**

27 This work was supported by an Early Career Faculty grant from NASA's Space Technology
28 Research Grants Program under Award No. 80NSSC18K1505. The characterization of IL-CO₂

1 binding and self-diffusivity corresponding to DAC relevant conditions were supported by the U.S.
2 Department of Energy, Office of Science, Basic Energy Science under award Number DE-
3 SC0022214. The authors would like to thank Dr. Ruizhi Pang and Dr. W.S. Winston Ho for
4 providing the *b*PES/PET substrate. The authors acknowledge the Northeast Ohio High Field NMR
5 Facility, Swagelok Center for Surface Analysis of Materials (SCSAM) for the access to SEM, and
6 the Soft Matter Characterization Laboratory for the access to TGA at Case Western Reserve
7 University.

8

9

1 REFERENCES

- 2 1 J. C. Knox, *47th Int. Conf. Environ. Syst.*, 2017, ICES-2017-209.
- 3 2 R. Huang, J. T.-M. Richardson, G. Belancik and D. Jan, *47th Int. Conf. Environ. Syst.*, 2017,
4 ICES-2017-116.
- 5 3 D. G. Madden, H. S. Scott, A. Kumar, K. Chen, R. Sanii, A. Bajpai, M. Lusi, T. Curtin, J. J.
6 Perry, M. J. Zaworotko and T. Curtin, *Philos. Trans. R. Soc. A Math. Phys. Eng. Sci.*, 2017,
7 **375**, 2084–2094.
- 8 4 J. C. Knox, *48th Int. Conf. Environ. Syst.*, 2018, ICES-2018-215.
- 9 5 Overview of Greenhouse Gases, [https://www.epa.gov/ghgemissions/overview-](https://www.epa.gov/ghgemissions/overview-greenhouse-gases)
10 [greenhouse-gases](https://www.epa.gov/ghgemissions/overview-greenhouse-gases).
- 11 6 National Academies, *Negative Emissions Technologies and Reliable Sequestration: A*
12 *Research Agenda (2019)*, 2019.
- 13 7 K. Z. House, A. C. Baclig, M. Ranjan, E. A. Van Nierop, J. Wilcox and H. J. Herzog, *Proc.*
14 *Natl. Acad. Sci. U. S. A.*, 2011, **108**, 20428–20433.
- 15 8 R. P. Lively and M. J. Realff, *AIChE J.*, 2016, **62**, 3699–3705.
- 16 9 M. V. Paragano and J. Kolmas, *45th Int. Conf. Environ. Syst.*, 2015, ICES-2015-112.
- 17 10 F. Zeman, *Environ. Sci. Technol.*, 2007, **41**, 7558–7563.
- 18 11 M. Erans, E. S. Sanz-Pérez, D. P. Hanak, Z. Clulow, D. M. Reiner and G. A. Mutch, *Energy*
19 *Environ. Sci.*, 2022, **15**, 1360–1405.
- 20 12 R. Custelcean, N. J. Williams, K. A. Garrabrant, P. Agullo, F. M. Brethomé, H. J. Martin and
21 M. K. Kidder, *Ind. Eng. Chem. Res.*, 2019, **58**, 23338–23346.
- 22 13 J. K. Stolaroff, D. W. Keith and G. V. Lowry, *Environ. Sci. Technol.*, 2008, **42**, 2728–2735.
- 23 14 K. Lackner, H.-J. Ziock and P. Grimes, in *Conference: 24th Annual Technical Conference on*
24 *Coal Utilization and Fuel Systems, Clearwater, FL (US)*, Clearwater, Florida, 1999.
- 25 15 A. Holewinski, M. A. Sakwa-Novak and C. W. Jones, *J. Am. Chem. Soc.*, 2015, **137**, 11749–
26 11759.
- 27 16 A. R. Sujan, S. H. Pang, G. Zhu, C. W. Jones and R. P. Lively, *ACS Sustain. Chem. Eng.*, 2019,
28 **7**, 5264–5273.
- 29 17 S. Bali, M. A. Sakwa-Novak and C. W. Jones, *Colloids Surfaces A Physicochem. Eng. Asp.*,

- 1 2015, **486**, 78–85.
- 2 18 T. Wang, K. S. Lackner and A. Wright, *Environ. Sci. Technol.*, 2011, **45**, 6670–6675.
- 3 19 X. Shi, H. Xiao, H. Azarabadi, J. Song, X. Wu, X. Chen and K. S. Lackner, *Angew. Chemie -*
4 *Int. Ed.*, 2020, **59**, 6984–7006.
- 5 20 E. A. Van Nierop, S. Hormoz, K. Z. House and M. J. Aziz, *Energy Procedia*, 2011, **4**, 1783–
6 1790.
- 7 21 Y. Duan and D. C. Sorescu, *J. Chem. Phys.*, 2010, **133**, 1–11.
- 8 22 S. T. Hwang, *AIChE J.*, 2004, **50**, 862–870.
- 9 23 H. B. Park, J. Kamcev, L. M. Robeson, M. Elimelech and B. D. Freeman, *Science (80-.)*,
10 2017, 356, 1138–1148.
- 11 24 W. J. Koros and C. Zhang, *Nat. Mater.*, 2017, **16**, 289–297.
- 12 25 I. Kammakam, K. E. O’Harra, E. M. Jackson and J. E. Bara, *Polymer (Guildf)*, ,
13 DOI:10.1016/j.polymer.2020.123239.
- 14 26 A. R. Nabais, R. O. Francisco, V. D. Alves, L. A. Neves and L. C. Tomé, *Membranes (Basel)*,
15 2021, **11**, 1–19.
- 16 27 I. Kammakam, J. E. Bara, E. M. Jackson, J. Lertxundi, D. Mecerreyes and L. C. Tomé, *ACS*
17 *Sustain. Chem. Eng.*, 2020, **8**, 5954–5965.
- 18 28 J. Liu, S. Zhang, D. en Jiang, C. M. Doherty, A. J. Hill, C. Cheng, H. B. Park and H. Lin, *Joule*,
19 2019, **3**, 1881–1894.
- 20 29 S. Tachibana, K. Hashimoto, H. Mizuno, K. Ueno and M. Watanabe, *Polymer (Guildf)*,
21 2022, **241**, 124533.
- 22 30 Z. Huang, C. Yin, T. Corrado, S. Li, Q. Zhang and R. Guo, *Chem. Mater.*, 2022, **34**, 2730–
23 2742.
- 24 31 T. J. Corrado, Z. Huang, D. Huang, N. Wamble, T. Luo and R. Guo, *Proc. Natl. Acad. Sci. U.*
25 *S. A.*, 2021, **118**, 1–7.
- 26 32 J. G. Seong, W. H. Lee, J. Lee, S. Y. Lee, Y. S. Do, J. Y. Bae, S. J. Moon, C. H. Park, H. J. Jo, J.
27 S. Kim, K. R. Lee, W. S. Hung, J. Y. Lai, Y. Ren, C. J. Roos, R. P. Lively and Y. M. Lee, *Sci.*
28 *Adv.*, 2021, **7**, 1–11.
- 29 33 I. Rose, C. G. Bezzu, M. Carta, B. Comesanã-Gándara, E. Lasseguette, M. C. Ferrari, P.

- 1 Bernardo, G. Clarizia, A. Fuoco, J. C. Jansen, K. E. Hart, T. P. Liyana-Arachchi, C. M. Colina
2 and N. B. McKeown, *Nat. Mater.*, 2017, **16**, 932–937.
- 3 34 L. Hu, V. T. Bui, A. Krishnamurthy, S. Fan, W. Guo, S. Pal, X. Chen, G. Zhang, Y. Ding, R. P.
4 Singh, M. Lupion and H. Lin, *Sci. Adv.*, 2022, **8**, 27–29.
- 5 35 B. Comesaña-Gándara, J. Chen, C. G. Bezzu, M. Carta, I. Rose, M. C. Ferrari, E. Esposito, A.
6 Fuoco, J. C. Jansen and N. B. McKeown, *Energy Environ. Sci.*, 2019, **12**, 2733–2740.
- 7 36 B. W. Rowe, L. M. Robeson, B. D. Freeman and D. R. Paul, *J. Memb. Sci.*, 2010, **360**, 58–
8 69.
- 9 37 L. M. Robeson, *J. Memb. Sci.*, 2008, **320**, 390–400.
- 10 38 A. Klemm, Y. Y. Lee, H. Mao and B. Gurkan, *Front. Chem.*, 2020, **8**, 1–8.
- 11 39 Y. Han and W. S. W. Ho, *Ind. Eng. Chem. Res.*, 2020, **59**, 5340–5350.
- 12 40 E. Kamio, M. Tanaka, Y. Shirono, Y. Keun, F. Moghadam, T. Yoshioka, K. Nakagawa and H.
13 Matsuyama, *Ind. Eng. Chem. Res.*, 2020, **59**, 2083–2092.
- 14 41 Y. Han, D. Wu and W. S. W. Ho, *J. Memb. Sci.*, 2018, **567**, 261–271.
- 15 42 S. Zhang, H. Li, H. Li, B. Sengupta, S. Zha, S. Li and M. Yu, *Adv. Funct. Mater.*, 2020, **30**,
16 2002804.
- 17 43 S. Janakiram, F. Santinelli, R. Costi, A. Lindbråthen, G. M. Nardelli, K. Milkowski, L.
18 Ansaloni and L. Deng, *Chem. Eng. J.*, 2021, **413**, 127405.
- 19 44 S. Janakiram, J. L. Martín Espejo, X. Yu, L. Ansaloni and L. Deng, *J. Memb. Sci.*, 2020, **616**,
20 118626.
- 21 45 J. Zhang, E. Kamio, A. Matsuoka, K. Nakagawa, T. Yoshioka and H. Matsuyama, *Ind. Eng.*
22 *Chem. Res.*, 2021, **60**, 12640–12649.
- 23 46 J. Zhang, E. Kamio, M. Kinoshita, A. Matsuoka, K. Nakagawa, T. Yoshioka and H.
24 Matsuyama, *Ind. Eng. Chem. Res.*, 2021, **60**, 12698–12708.
- 25 47 Y. Han and W. S. W. Ho, *J. Membr. Sci. Lett.*, 2022, **2**, 100014.
- 26 48 X. Deng, C. Zou, Y. Han, L.-C. Lin and W. S. W. Ho, *J. Phys. Chem. C*, 2020, **124**, 25322–
27 25330.
- 28 49 A. Matsuoka, S. Taniguchi, E. Kamio and H. Matsuyama, *Ind. Eng. Chem. Res.*, ,
29 DOI:10.1021/acs.iecr.1c00615.

- 1 50 D. T. Wickham, K. J. Gleason, J. R. Engel, S. W. Cowley and C. Chullen, *43th Int. Conf.*
2 *Environ. Syst.*, 2013, 1–24.
- 3 51 D. T. Wickham, .
- 4 52 S. Fujikawa, R. Selyanchyn and T. Kunitake, *Polym. J.*, 2021, **53**, 111–119.
- 5 53 C. Castel, R. Bounaceur and E. Favre, *Front. Chem. Eng.*, 2021, **3**, 1–15.
- 6 54 S. Marius, S. E. M., I. W. F., D. Jing, S. P. M., D. Liyuan and S. R. J., *Science (80-.)*, 2022,
7 **376**, 90–94.
- 8 55 B. Belaissaoui, E. Lasseguette, S. Janakiram, L. Deng and M. C. Ferrari, *Membranes*
9 *(Basel)*., 2020, **10**, 1–23.
- 10 56 Y. Y. Lee and B. Gurkan, *J. Memb. Sci.*, 2021, **638**, 119652.
- 11 57 R. Pang, K. K. Chen, Y. Han and W. S. W. Ho, *J. Memb. Sci.*, 2020, **612**, 118443.
- 12 58 Y. Y. Lee, D. Penley, A. Klemm, W. Dean and B. Gurkan, *ACS Sustain. Chem. Eng.*, ,
13 DOI:10.1021/acssuschemeng.0c07217.
- 14 59 Y. Y. Lee, K. Edgehouse, A. Klemm, H. Mao, E. Pentzer and B. Gurkan, *ACS Appl. Mater.*
15 *Interfaces*, 2020, **12**, 19184–19193.
- 16 60 N. A. Ramli, N. A. Hashim and M. K. Aroua, *Chem. Eng. Commun.*, 2018, **205**, 295–310.
- 17 61 H. Tokuda, K. Hayamizu, K. Ishii, M. A. B. H. Susan and M. Watanabe, *J. Phys. Chem. B*,
18 2004, **108**, 16593–16600.
- 19 62 S. M. Green, M. E. Ries, J. Moffat and T. Budtova, *Sci. Rep.*, 2017, **7**, 1–12.
- 20 63 A. Radhi, K. A. Le, M. E. Ries and T. Budtova, *J. Phys. Chem. B*, 2015, **119**, 1633–1640.
- 21 64 R. Pang, Y. Yang, Y. Han, K. K. Chen and W. S. W. Ho, *J. Memb. Sci.*, 2022, **654**, 120547.
- 22 65 W. Ying, J. Cai, K. Zhou, D. Chen, Y. Ying, Y. Guo, X. Kong, Z. Xu and X. Peng, *ACS Nano*,
23 2018, **12**, 5385–5393.
- 24 66 X. Wan, K. Zhang, T. Wan, Y. Yan, Z. Ye and X. Peng, *J. Memb. Sci.*, 2022, **652**, 120475.
- 25 67 M. Dong, K. Zhang, X. Wan, S. Wang, S. Fan, Z. Ye, Y. Wang, Y. Yan and X. Peng, *Small*,
26 2022, **18**, 2108026.
- 27 68 M. Dong, K. Zhang, X. Wan, Z. Fang, Y. Hu, Z. Ye, Y. Wang, Z. Li and X. Peng, *Appl. Mater.*
28 *Today*, 2022, **27**, 101458.
- 29 69 R. Pang, Y. Han, K. K. Chen, Y. Yang and W. S. W. Ho, *Appl. Energy*, 2022, **311**, 118624.

- 1 70 X. Deng, Y. Han, L. C. Lin and W. S. W. Ho, *J. Phys. Chem. C*, 2022, **126**, 3661–3670.
- 2 71 A. Matsuoka, A. Otani, E. Kamio and H. Matsuyama, *Sep. Purif. Technol.*, 2022, **280**,
- 3 119847.
- 4